Core–Shell Nanoparticles As Building Blocks for the Bottom-Up Production of Functional Nanocomposites: PbTe–PbS Thermoelectric Properties

Maria Ibáñez,[†] Reza Zamani,[‡,§] Stéphane Gorsse,[⊥] Jiandong Fan,[‡] Silvia Ortega,[†] Doris Cadavid,[‡] Joan Ramon Morante,[†,‡] Jordi Arbiol,[§,∥] and Andreu Cabot[†,‡,*]

[†]Departament d'Electrònica, Universitat de Barcelona, Barcelona 08028, Spain, [‡]Catalonia Institute for Energy Research—IREC, Jardí de les Dones de Negre 1, Sant Adrià de Besòs, Barcelona, 08930, Spain, [§]Institut de Ciència de Materials de Barcelona, ICMAB-CSIC, Campus de la UAB, Bellaterra, 08193, Spain, [⊥]CNRS, Université de Bordeaux, ICMCB, 87 Avenue du Docteur Albert Schweitzer, 33608 Pessac Cedex, France, and [∥]Institució Catalana de Recerca i Estudis Avançats (ICREA), 08010 Barcelona, Spain

ABSTRACT The bottom-up assembly of nanocrystals provides access to a three-dimensional composition control at the nanoscale not attainable by any other technology. In particular, colloidal nanoheterostructures, with intrinsic multiphase organization, are especially appealing building blocks for the bottom-up production of nanocomposites. In the present work, we use PbTe–PbS as the model material system and thermoelectricity as the paradigmatic application to investigate the potential of the bottom-up assembly of core–shell nanoparticles to produce functional nanocomposites. With this goal in mind, a rapid, high-yield and scalable colloidal synthetic route to prepare grams of PbTe@PbS core–shell nanoparticles with unprecedented narrow size distributions and exceptional composition control is detailed. PbTe@PbS nanoparticles were used as building blocks for the bottom-up production of PbTe–PbS nanocomposites with tuned composition. In such PbTe–PbS nanocomposites, synergistic nanocrystal doping effects result in up to 10-fold higher electrical conductivities than in pure PbTe and PbS nanomaterials. At the same time, the acoustic impedance mismatch between PbTe and PbS phases and a partial phase alloying provide PbTe–PbS nanocomposites with strongly reduced thermal conductivities. As a result, record thermoelectric figures of merit (ZT) of ~1.1 were obtained from undoped PbTe and PbS phases at 710 K. These high ZT values prove the potential of the proposed processes to produce efficient functional nanomaterials with programmable properties.

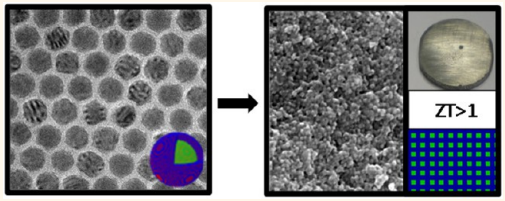

KEYWORDS: colloidal nanoparticles · thermoelectricity · nanomaterial · nanocomposite · heterostructures · core–shell nanoparticles

To control material properties and to understand mechanisms and phenomena at the atomic scale are two main ambitious goals of the current research and development of advanced functional materials. One step above that, industrial innovation requires the development of cost-effective processes able to transform this control and understanding into optimized or novel products. In this context, the bottom-up assembly of nanoparticles (NP) offers a unique potential not only to perform fundamental studies with precisely controlled material parameters but also to produce artificial materials with functional properties by design in a cost-effective manner. In this scenario, the outstanding degree of control over size, shape, phase, and composition that colloidal synthesis methods have achieved makes colloidal NPs particularly suitable building blocks to prepare functional nanomaterials.[1−6] At the same time, the advantageous processability, low synthesis temperatures, large production rates, and high production yields of solution-processing methods offer unpaired opportunities to fabricate low-cost devices.

An especially attractive application for nanomaterials and nanotechnology researchers and developers is thermoelectricity. Thermoelectric energy conversion comprises two very appealing attributes: an enormous potential for economical and social impact, and the need for material control at the

* Address correspondence to acabot@irec.cat.

Received for review December 24, 2012 and accepted February 28, 2013.

Published online February 28, 2013
10.1021/nn305971v

nanoscale to exploit this potential. Thermoelectric energy conversion devices have an ample range of current and potential applications: from precise temperature control in countless areas to energy harvesting for autonomous sensing devices and waste heat recovery from industrial and domestic processes. However, in spite of their broad range of applications and their unique advantages, thermoelectric devices are banned from multiple potential markets because of their relatively low efficiencies. Nanomaterials may have the key to open these markets to thermoelectricity. To date, nearly all high figure of merit thermoelectrics are nanostructured.[7−9] The confinement of the lattice dimensions to the nanometer scale allows improving thermoelectrics efficiency by promoting phonon scattering at crystal interfaces. At the same time, the selective scattering of the low-energy charge carriers at crystal interfaces provides a path toward higher Seebeck coefficients.[10−13]

Record thermoelectric figures of merit, up to ZT = 2.4, have been reported for superlattices produced by thin film technologies such as molecular beam epitaxy.[14,15] However, because of their very low growth rates and material yields, such vacuum-based bottom-up processing technologies are neither particularly low-cost nor versatile for large-scale production. These processes do not allow the production of nanocomposites in bulk form either. Recently, cost-effective and scalable methods suitable to produce high-efficiency thermoelectric nanocomposites have been developed. They are based on the spontaneous formation of nanoscale inclusions by controlling the thermal history of solid solutions.[16−18] PbTe−PbS nanocomposites are one of the best performing thermoelectric materials obtained by this method.[18−23] However, while such an approach is excellent in particular systems, it is not versatile in composition and it lacks control over the size, composition, and phase of the nanocrystalline domains.

The bottom-up assembly of nanocrystal building blocks is becoming a serious alternative to produce thermoelectric nanomaterials.[24−33] No other technology has the potential to produce nanomaterials with a comparable level of control over the size, shape, composition, and phase of the crystal domains at the nanoscale.[34−40] In this scenario, nanoheterostructures are particularly interesting building blocks, as they allow producing highly homogeneous bulk nanocomposites in an easier manner. The availability of such multiphase building blocks provides unprecedented degrees of experimental freedom to create nanocomposites with programmed properties. The rational design and engineering of such bottom-up assembled nanocomposites will allow developing the next generation of energy conversion and storage devices having enhanced performances and lower costs.

We aim to demonstrate the potential of the bottom-up assembly of nanoheterostructures to produce bulk nanocomposites with enhanced functional properties. In particular, we target the use of PbTe@PbS core−shell NPs to produce PbTe−PbS nanocomposites with high thermoelectric figures of merit. With this goal in mind, we present here a rapid, high-yield, and scalable colloidal synthetic route to prepare PbTe@PbS NPs with unprecedented narrow size distributions and exceptional control over their composition. PbTe@PbS core−shell NPs obtained by this method were used to produce $(PbTe)_{1-x}(PbS)_x$ nanocomposites with tuned composition (Scheme 1). The structural, chemical, and thermoelectric properties of the obtained nanocomposites are presented and discussed.

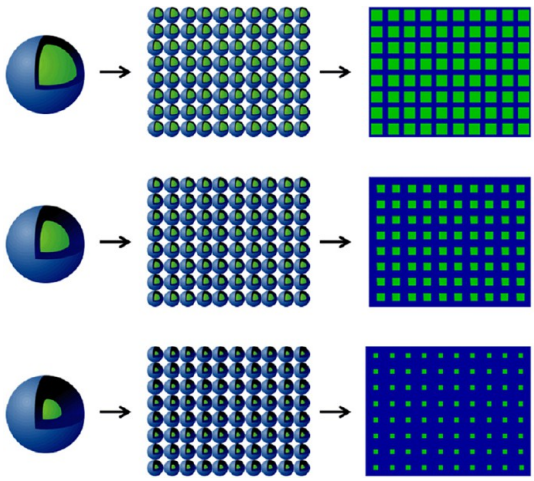

Scheme 1. Steps for the production of nanocomposites from the bottom-up assembly of core−shell nanoparticles with different shell thicknesses: (i) core−shell nanoparticle preparation; (ii) nanoparticle assembly; and (iii) annealing to produce a dense nanocomposite.

RESULTS AND DISCUSSION

PbTe@PbS Nanoparticles. Colloidal synthetic strategies to produce nanoheterostructures are generally highly elaborated.[34,38,41−57] To date, most colloidal synthetic routes to produce core−shell nanoparticles are based on two-pot processes not well suited for production scale up. Moreover, most previous efforts to prepare core−shell NPs were focused on the production of shells just thick enough to passivate the core surface and improve photoluminescence or provide biocompatibility.

We aimed at the development of scalable synthetic routes suitable for the production of nanoheterostructures and bulk nanocomposites in an industrially relevant manner. For this purpose, we designed a one-pot two-step procedure to prepare core−shell NPs at the multigram scale. The one-pot procedure facilitates up-scaling, maximizes production yield, and minimizes the processing time and the number of purification steps. An additional advantage of one-pot processes is that they allow minimizing the core oxidation.

Our one-pot two-step procedure to prepare PbTe@PbS NPs is as follows. In a first step, PbTe NPs

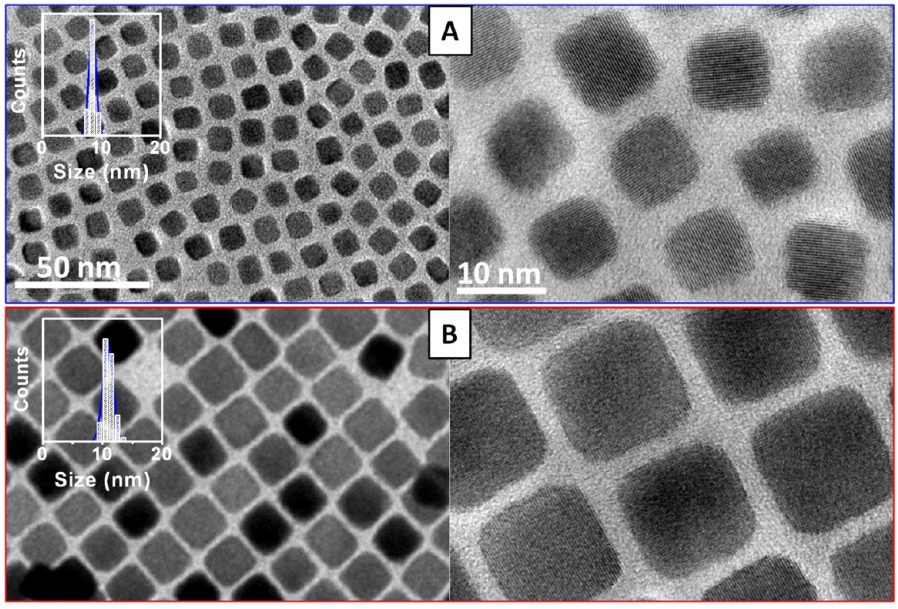

Figure 1. TEM micrographs of two batches of PbTe nanoparticles having average sizes of 8.5 ± 0.7 nm (A) and 11 ± 1 nm (B). Insets display the histograms with the particle size distributions.

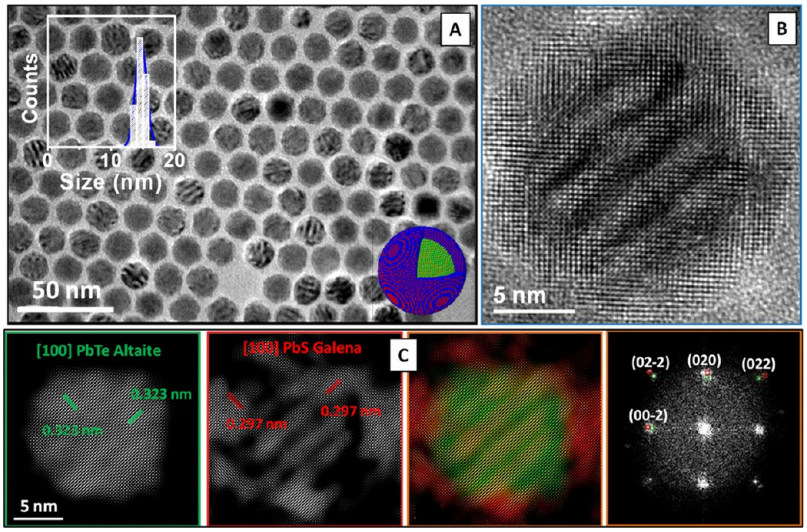

Figure 2. (A) TEM micrograph of $(PbTe)_{0.28}@(PbS)_{0.72}$ core−shell nanoparticles with crystalline PbS shells. Inset displays the histogram of the particle size distribution. (B) HRTEM micrograph of a $(PbTe)_{0.28}@(PbS)_{0.72}$ core−shell nanoparticle. (C) Power spectrum analysis of the same $(PbTe)_{0.28}@(PbS)_{0.72}$ nanoparticle and PbTe and PbS crystallographic color maps.

were prepared by reacting Pb oleate with TOP:Te in octadecene. Figure 1 shows representative transmission electron microscopy (TEM) micrographs of the cubic PbTe NPs produced in two different 1 g batches. In spite of the relatively high production scale, particle size distributions with exceptionally low dispersions, <10%, were systematically obtained (Figure 1 insets). In a second step, without purifying or exposing the PbTe NPs to air, the sulfur precursor was added to the crude solution containing the PbTe NPs at room temperature. Then, the temperature was gradually increased to 80 °C at 1.7 °C/min. We found that heating rates, reaction temperatures, and sulfur source reactivity determined the mechanism of formation of the PbS shell. Large precursor reactivities or high reaction temperatures promoted the Te replacement by S within the PbTe core or the nucleation of independent PbS crystals. Reaction conditions had to be carefully adjusted to promote the PbS shell growth on the PbTe core surface. A solution of thioacetamide in dimethylformamide was proven to be the most effective S source for PbS shell growth. Figure 2A shows a representative TEM micrograph of the PbTe@PbS core−shell NPs produced. The detailed procedure systematically yielded core−shell NPs with narrow size distributions, <10% (Figure 2A inset). It must be pointed out that all the NPs characterized and shown in the present work were obtained from relatively large scale

synthesis, producing up to 1−1.5 g of material in a single pot. More details on the materials synthesis can be found in the Materials and Methods section.

High-resolution TEM (HRTEM) micrographs revealed cores and shells produced by this method to be single crystalline (Figure 2B). Double points marked by red and green circles in the power spectrum analysis (FFT) resulted from the shell and core lattices, respectively (Figure 2C). Core and shell had the same crystal structure (S.G.: *Fm*3*m*) with identical positions of the atoms in the unit cell but different cell parameters. The lattice spacing shown in Figure 2C corresponds to the (200) planes in altaite PbTe (0.323 nm, JCDP: 00-038-1435) and galena PbS (0.297 nm, JCDP: 00-005-0592). The coexistence of both crystal structures was confirmed by X-ray diffraction (XRD). Figure 3 displays the XRD patterns of the $(PbTe)_{1-x}@(PbS)_x$ (x = 0, 0.32, 0.40, 0.49, 0.72, 1) NPs with crystalline PbS shells produced. No evidence of alloying, oxidation, or the presence of a $PbTe_yS_{1-y}$ interface layer could be obtained by either HRTEM or XRD.

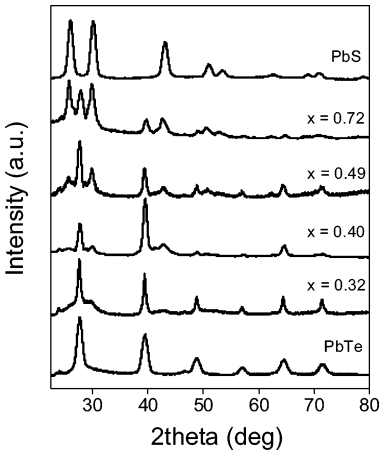

Figure 3. XRD patterns of $(PbTe)_{1-x}@(PbS)_x$ core−shell nanoparticles with x = 0, 0.32, 0.40, 0.49, 0.72, and 1.

TEM micrographs of the core−shell NPs showed variable contrasts within each NP. A range of different contrast patterns was observed. We attributed these contrast variations to different Moiré patterns produced depending on the NP orientation with respect to the electron beam. Moiré patterns allowed us to characterize in more detail the crystal interface between the core and shell lattices in PbTe@PbS NPs. Moiré patterns depend on the mismatch between cell parameters and the relative orientation between the two superimposed lattices and between the lattices and the electron beam. Figure 4 displays experimental and simulated HRTEM images of NPs with different Moiré patterns. Circular-like patterns (Figure 4A) are characteristic of Moiré fringes occurring along both x and y axes when the NPs are perfectly oriented along the [100] zone axis. This is quite improbable due to the random distribution of the NPs when lying on the carbon grid, and thus few NPs showed such circular patterns. Most NPs were characterized by stripe-like Moiré fringes (Figure 4B, C, D). Stripe-like patterns are generally associated with the superposition of two lattices with the same cell parameter in one direction and a slight difference in another. However, stripe-like patterns were explained here by the slight rotation of the NP from the exact zone axis. Figure 4B shows the experimental and simulated core−shell NP rotated 2° along the [010] axis from the [100] view direction, and Figure 4C the same but with 5° rotations. Figure 4D shows the result of rotating 2° along [010] and 2° along [001]. From a thorough analysis of the Moiré fringes of

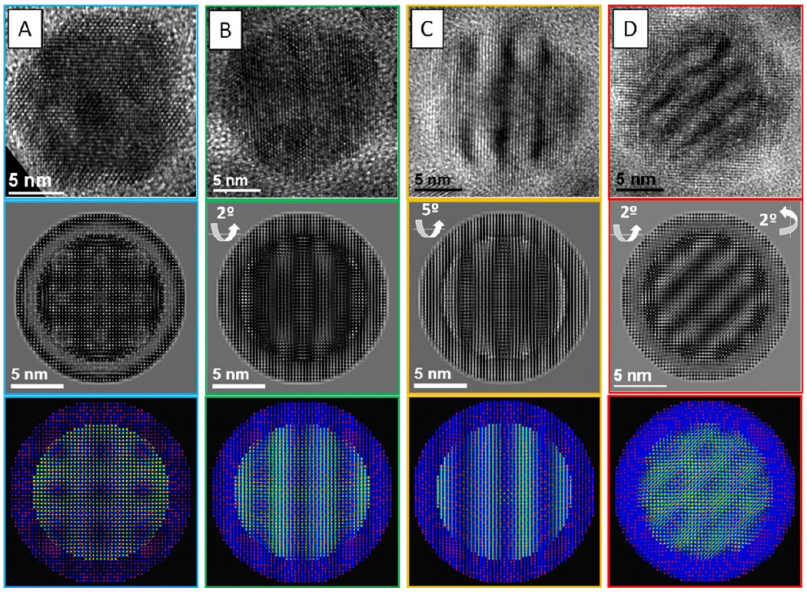

Figure 4. Experimental images, simulated HRTEM micrographs, and atomic models of various PbTe@PbS core−shell nanoparticles showing varied Moiré fringes associated with different orientations with respect to the [100] zone axis.

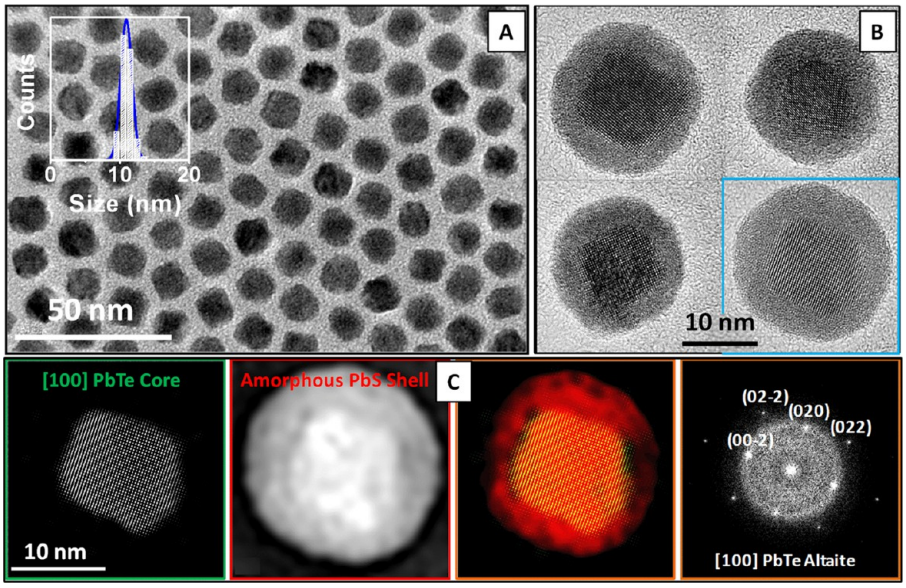

Figure 5. (A) TEM micrograph of $(PbTe)_{0.25}@(PbS)_{0.75}$ core−shell nanoparticles having amorphous PbS shells. Inset displays the histogram of the particle size distribution. (B) HRTEM micrograph of a few $(PbTe)_{0.25}@(PbS)_{0.75}$ core−shell nanoparticles. (C) Power spectrum analysis of a $(PbTe)_{0.25}@(PbS)_{0.75}$ nanoparticle and PbTe and PbS crystallographic color maps.

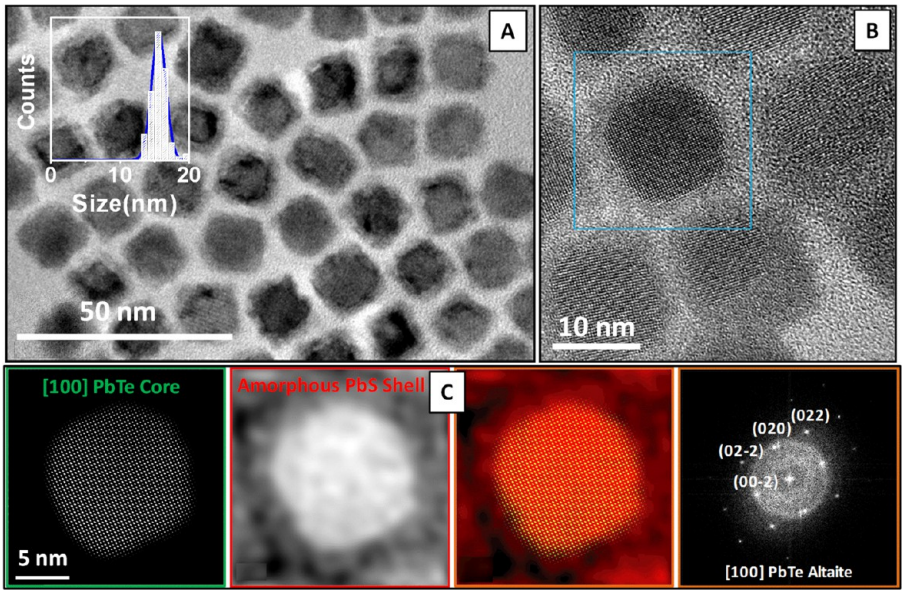

Figure 6. (A) TEM micrograph of $(PbTe)_{0.60}@(PbS)_{0.40}$ core−shell nanoparticles with quasi-cubic shapes. Inset displays the histogram of the particle size distribution. (B) HRTEM micrograph of a few $(PbTe)_{0.60}@(PbS)_{0.40}$ core−shell nanoparticles. (C) Power spectrum analysis of a $(PbTe)_{0.60}@(PbS)_{0.40}$ nanoparticle and PbTe and PbS crystallographic color maps.

a large number of PbTe@PbS NPs, we concluded that all the cores and shell lattices had the same epitaxial relationship: $(010)[100]_{PbTe}//(010)[100]_{PbS}$.

The shell crystallinity could be controlled by varying the reaction kinetics during shell formation. PbTe@PbS core−shell NPs with amorphous PbS shells were produced by boosting PbS nucleation at multiple PbTe surface sites when injecting the S precursor at relatively high temperatures: 80 °C (Figure 5, Supporting Information, SI, Figure S1). Additionally, the shape of the PbTe@PbS NPs was controlled by adjusting the degree of faceting of the PbTe core and the thickness of the shell. Small PbTe cores were quasi cubic with slightly rounded corners. The growth of thick PbS shells on the surface of such rounded PbTe nanocrystals resulted in spherical core−shell NPs (Figures 3, 5). In contrast, the growth of relatively thin PbS shells on the surface of larger and highly faceted PbTe cores resulted in quasi-cubic PbTe@PbS NPs (Figure 6). Figure S2 displays a scheme summarizing the synthetic results in terms of crystallinity and shape.

Most importantly, the developed method allowed us to produce core−shell NPs with large shell thickness (>5 nm) and an independent control over the NP size

and composition. Having in mind their posterior thermoelectric characterization, we produced a set of $(PbTe)_{1-x}@(PbS)_x$ NPs with identical size but different PbTe/PbS ratios. To accomplish this goal, we synthesized PbTe cores with different diameters by varying the PbTe growth temperature between 160 and 190 °C but maintaining the same amounts of Pb oleate and surfactants from batch to batch. Thus, large/small PbTe cores obtained at high/low temperatures involved small/large amounts of Pb oleate left in solution to react with S in the second step. In this way, we limited the shell growth by the concentration of Pb monomer, obtaining core−shell NPs with the same diameter for all compositions. Figure 7 displays representative TEM micrograph of the set of $(PbTe)_{1-x}@(PbS)_x$ NPs produced.

PbTe−PbS Nanocomposite Formation. The set of PbTe@PbS core−shell NPs with similar overall size but different PbTe/PbS ratios displayed in Figure 7 was used to produce a set of $(PbTe)_{1-x}(PbS)_x$ nanocomposites with x = 0.32, 0.40, 0.49, and 0.72. As references, we also produced pure PbTe and PbS nanomaterials from the processing of PbTe (11.2 ± 1.0 nm) and PbS (6.1 ± 0.4 nm) NPs (Figures S3 and S4). Once prepared, $(PbTe)_{1-x}@(PbS)_x$ (x = 0, 0.32, 0.40, 0.49,0.72, 1) NPs were purified by multiple precipitation and redispersion steps until no redispersion was possible. At this point, most of the organic ligands used to control the size and shape of the NPs during synthesis had been removed. Purified $(PbTe)_{1-x}@(PbS)_x$ NPs were dried under vacuum to obtain a dark gray nanopowder. This nanopowder was annealed at 500 °C for 1 h under a dry argon flow to completely remove residual organics. Elemental analysis showed the presence of approximately 1% of carbon in the annealed materials. The annealed nanopowders were pressed under 2 tons of force at room temperature to produce dense $(PbTe)_{1-x}(PbS)_x$ pellets. The obtained nanocrystalline pellets were silver-metallic in appearance and had relative densities of 80%. Table 1 summarizes the basic characteristics of the $(PbTe)_{1-x}(PbS)_x$ nanocomposites produced.

The characterization of the annealing effect on the nanocomposite structure was both challenging but also necessary to understand the thermoelectric performance of the obtained materials. As proven by SEM-EDX and HRTEM (Figure 8), the composition of the final nanomaterials was highly homogeneous at the micrometer scale but contained a uniform distribution of compositional inhomogeneities at the nanometer scale. HRTEM analysis of the nanocomposites showed them to contain PbS and PbTe crystal nanodomains with sizes in the range 10−20 nm (Figure 8).

Figure 9 displays the XRD patterns of the set of $(PbTe)_{1-x}(PbS)_x$ nanomaterials studied. After the annealing treatment, reflections from PbTe and PbS phases still dominated the XRD patterns. However, two new weak crystallographic reflections were observed.

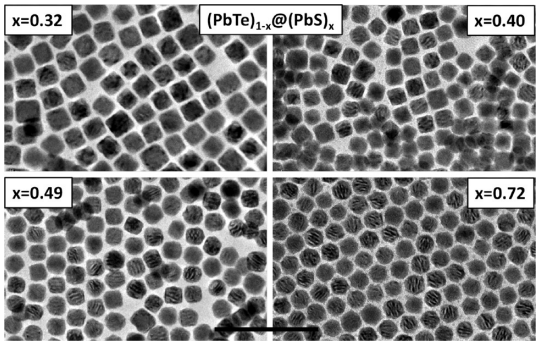

Figure 7. TEM micrographs of the $(PbTe)_{1-x}@(PbS)_x$ nanoparticles used for thermoelectric characterization. Scale bar corresponds to 100 nm.

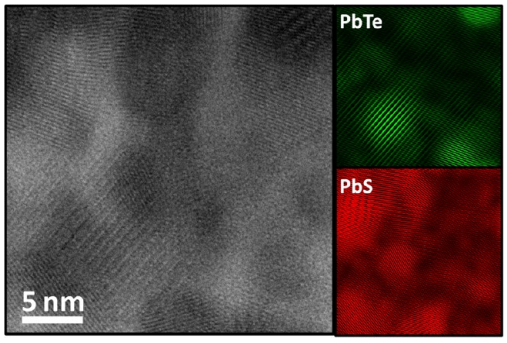

Figure 8. HRTEM micrograph and color crystallographic maps of $(PbTe)_{0.28}(PbS)_{0.72}$ nanocomposite: PbTe = green; PbS = red.

TABLE 1. Reaction Temperature (T_R), PbTe Average Core Size (d), PbTe@PbS Average Nanoparticle Size (D), Chalcogen Molar Content (Te, S), Sulfur Content in the Te-Rich Phase (y), and Te Content in the S-Rich Phase (z)

				chalcogen content (%)		y	z
$(PbTe)_{1-x}(PbS)_x$ x	T_R (°C)	PbTe d (nm)	PbTe@PbS D (nm)	Te	S	$PbTe_yS_{1-y}$	PbS_zTe_{1-z}
0	190	11.2 ± 1.0	11.2 ± 1.0	100	0	1	0
0.32	190	11.1 ± 1.0	14.4 ± 2.1	68.2	31.8	0.96	0.98
0.40	180	10.2 ± 0.8	14.2 ± 1.9	60.2	39.8	0.93	0.99
0.49	170	9.4 ± 0.9	14.3 ± 2.0	51.4	48.6	0.92	0.99
0.72	160	8.5 ± 0.7	14.1 ± 2.0	27.8	72.2	0.90	1
1	135	0	6.1 ± 0.4	0	100	0	1

The new XRD peaks were identified as the (101) and (110) plane reflections of PbO. Surprisingly, the presence of PbO was observed in all samples except pure PbTe. A significant amount of oxygen is usually observed at the surface of PbTe NPs when exposed to air even during very short periods of time.[27,58,59] Therefore, we tentatively associated the absence of the PbO phase reflections from the pure PbTe nanomaterial with the amorphous nature of the thin oxide layer potentially formed. The reason for the distinct crystallinity of the formed oxide over PbS and PbTe surfaces can be found in the different surface termination of the NPs prepared. On one hand, the surface of cubic or quasi-cubic PbTe nanocrystals was saturated with Te.[60] Oxidation of such Te-rich surfaces results in the formation of $PbTeO_3$.[61,62] Since no evidence for such a crystal structure was obtained by XRD or HRTEM, we speculate that such an oxide layer was amorphous or very thin. On the other hand, the surface of spherical PbS NPs like those obtained here is Pb-rich due to the preferential bonding of oleic acid to Pb sites.[63,64] The oxidation of the Pb-rich surface of PbS NPs most probably proceeded *via* the direct formation of PbO, which crystallized during the thermal treatment.

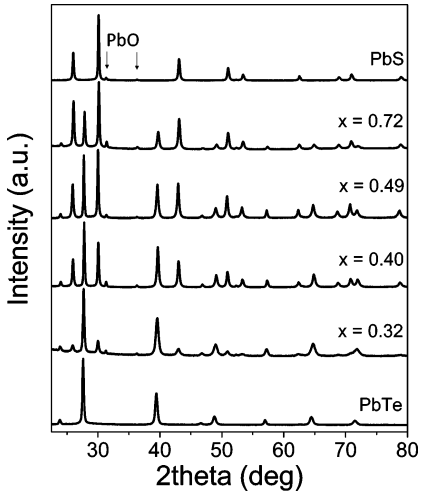

Figure 9. XRD patterns of the $(PbTe)_{1-x}(PbS)_x$ (x = 0, 0.32, 0.40, 0.49, 0.72, 1) nanomaterials.

While nanocomposites produced here conserved both PbTe and PbS diffraction patterns after the thermal treatment, we observed a slight shift of the PbTe and PbS reflections toward higher and lower angles, respectively. These shifts were associated with a partial alloying during annealing. The refined lattice parameters calculated from the XRD data are plotted as a function of the PbS content in Figure 10. Smaller lattice parameters were obtained when increasing the PbS concentration in $(PbTe)_{1-x}(PbS)_x$ nanocomposites. Figure 10 displays the lattice parameter trend considering Vergard's law for a complete solid solution. Following Vergard's law, the alloying ratio for both PbTe-rich and PbS-rich phases was calculated (Table 1). This alloying was limited to 10% in the Te-rich phase and to 2% in the S rich phase. This is consistent with the very limited miscibility of the PbTe−PbS system.[23,65−67]

Thermoelectric Properties. We characterized the electrical conductivity (σ), Seebeck coefficient (S), and thermal conductivity (κ) of the $(PbTe)_{1-x}(PbS)_x$ (x = 0, 0.32, 0.40, 0.49, 0.72, 1) nanomaterials in the temperature range from 320 to 710 K. Table 2 summarizes the thermoelectric properties of $(PbTe)_{1-x}(PbS)_x$ nanomaterials at 320 and 710 K.

Electrical Conductivity and Seebeck Coefficient. Figure 11 displays the electrical conductivity and Seebeck coefficient of $(PbTe)_{1-x}(PbS)_x$ nanomaterials. The evolution of the electrical conductivity with temperature clearly indicated that charge carrier scattering at grain boundaries and crystal interfaces played a dominant role.[13,27] Electrical conductivities activated through a surface energy barrier (E_a) can be expressed as follows:[68] $\sigma \propto T^{-1/2} \exp(-E_a/kT)$. The results from the fitting of this equation to our experimental data in the

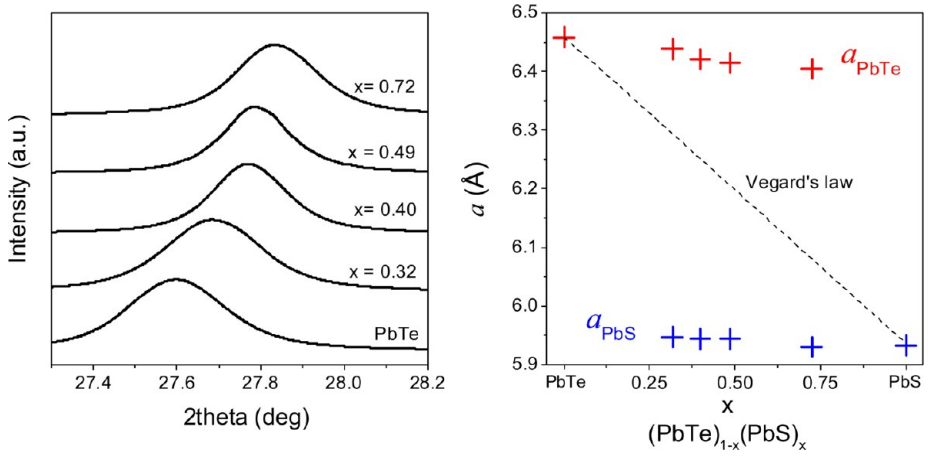

Figure 10. XRD patterns and calculated lattice parameters for PbTe- and PbS-rich phases as a function of the $(PbTe)_{1-x}(PbS)_x$ nanomaterial composition.

TABLE 2. Activation Energy for Electrical Transport in the Low-Temperature Range (E_a), Electrical Conductivity (σ), Thermopower (S), Porosity-Corrected Thermal Conductivity (κ^*), and Thermoelectric Figure of Merit ($ZT = T\sigma S^2/\kappa$) of $(PbTe)_{1-x}(PbS)_x$ Nanomaterials

x		σ (S m^{-1})		S (μV K^{-1})		κ^* (W m^{-1} K^{-1})		ZT	
$(PbTe)_{1-x}(PbS)_x$	E_a (meV)	320 K	710 K	320 K	710 K	320 K	710 K	320 K	710 K
0	83	55	2370	362	−270	2.2	1.20	10^{-3}	0.18
0.32	78	51	5510	184	−247	1.8	1.15	10^{-4}	0.37
0.40	81	9.0	4380	1	−259	1.5	0.91	10^{-4}	0.34
0.49	75	76	7730	−89	−232	0.85	0.61	10^{-4}	0.86
0.72	71	12	12530	−89	−185	0.69	0.53	10^{-4}	1.03
1	66	260	1180	−279	−306	1.2	0.77	10^{-2}	0.18

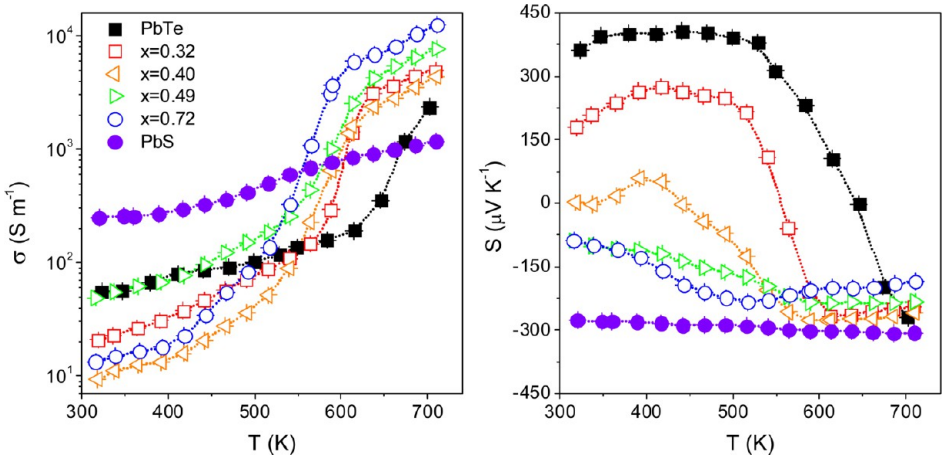

Figure 11. Electrical conductivity (σ) and Seebeck coefficient (S) for $(PbTe)_{1-x}(PbS)_x$ nanomaterials.

low-temperature range (T < 400 K) are displayed in Table 2. The highest activation energy of E_a = 83 meV was obtained for pure PbTe. This value is in the range of activation energies previously measured for this material (60 meV < E_a < 140 meV).[27,13] The energy barrier decreased with the PbS content within the $(PbTe)_{1-x}(PbS)_x$ nanocomposites (Figure 12). Pure PbS nanomaterials displayed the lowest energy barriers; E_a = 66 meV.

In the low-temperature regime, majority carriers in PbTe and PbS had opposite signs. While PbTe displayed p-type conductivity, PbS had an n-type character. When both phases were intermixed within $(PbTe)_{1-x}(PbS)_x$ nanocomposites, holes from PbTe and electrons from PbS compensated each other, resulting in lower electrical conductivities and lower absolute Seebeck coefficients than those of pure PbTe and PbS nanomaterials. In this low-temperature range, charge transport was dominated by holes in $(PbTe)_{1-x}(PbS)_x$ nanocomposites with $x \leq 0.4$ and by electrons in $(PbTe)_{1-x}(PbS)_x$ nanocomposites with higher PbS contents (x > 0.4).

In nanomaterials with energy-activated charge carrier mobilities, the increase of the average carrier kinetic energy with temperature eventually enables charge carriers to overcome the potential barrier. At this temperature, electrical conductivity is largely enhanced. In pure PbTe the boost of electrical conductivity was accompanied by an inversion of the majority carriers' charge sign (Figure 11). At around 520 K a strong decrease of the Seebeck coefficient, from positive to negative values, starts to take place in PbTe. This is associated with an increasingly higher density of electrons participating in the charge transport within this material. At around 650 K the electron contribution to the Seebeck coefficient compensated the hole contribution. Negative Seebeck coefficients were obtained at higher temperatures. In $(PbTe)_{1-x}(PbS)_x$ nanocomposites, charge carrier compensation occurred at lower temperatures. For $(PbTe)_{0.68}(PbS)_{0.32}$, the sign inversion in the Seebeck coefficient took place at around 550 K and for $(PbTe)_{0.60}(PbS)_{0.40}$ at just 450 K. In $(PbTe)_{1-x}(PbS)_x$ with x > 0.4 a step change of the Seebeck coefficient toward more negative values was also obtained in this temperature range. This sign inversion or step change in the Seebeck coefficient was accompanied by an increase in electrical conductivity in the temperature range from 450 to 650 K for all nanocomposites.

At relatively high temperature (T > 650 K), both PbTe and PbS displayed n-type conductivity. In this regime a synergistic contribution of the majority

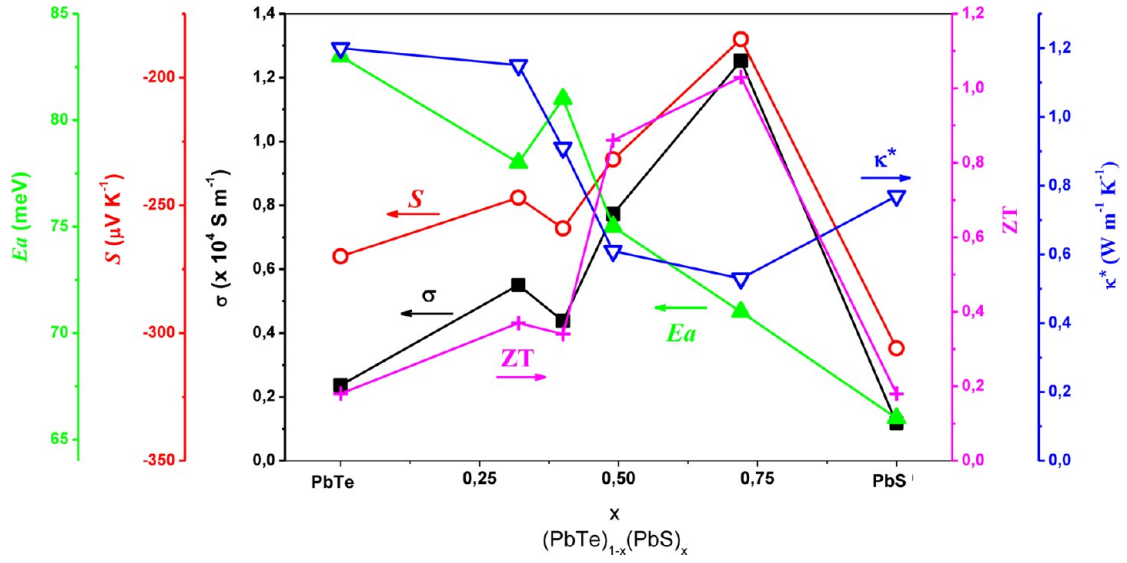

Figure 12. Electrical conductivity (σ), Seebeck coefficient (S), porosity-corrected thermal conductivity (κ*), and thermoelectric figure of merit (ZT) at 710 K and activation energy for electrical transport in the low-temperature range (E_a), as a function of the PbS concentration in $(PbTe)_{1-x}(PbS)_x$ nanomaterials.

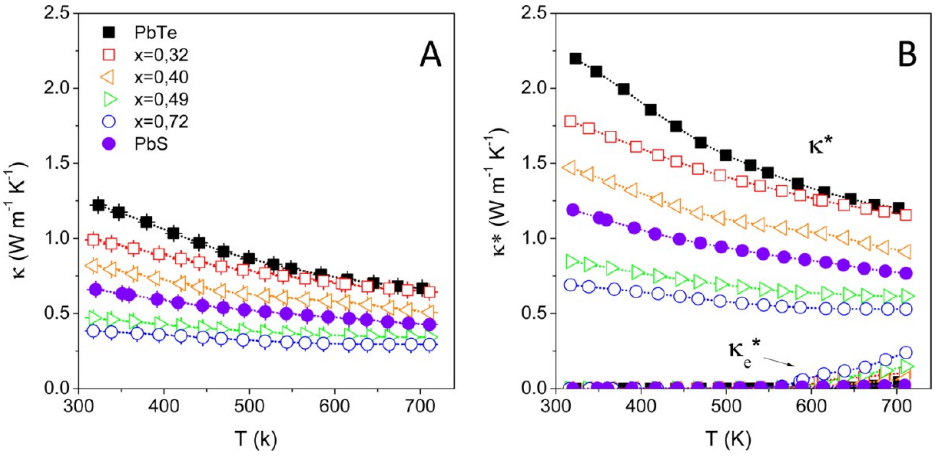

Figure 13. Thermal conductivity (A) and porosity-corrected thermal conductivity and electronic contribution to the corrected thermal conductivity (B) of $(PbTe)_{1-x}(PbS)_x$ nanomaterials.

charge carriers of both phases was observed, and much higher electrical conductivities were obtained for nanocomposites than for pure PbTe and PbS nanomaterials. In the high-temperature regime measured, the electrical conductivity of $(PbTe)_{1-x}(PbS)_x$ nanocomposites increased with the PbS content. The highest electrical conductivities were obtained for $(PbTe)_{0.28}(PbS)_{0.72}$. For this material electrical conductivities up to 10-fold larger than PbS were measured. Without intentional doping of any of the two phases, $(PbTe)_{0.28}(PbS)_{0.72}$ reached electrical conductivities up to 1.2×10^4 S m^{-1}. This value is just slightly lower than that reported by S. Johnsen *et al.* for 0.033% $PbCl_2$-doped $PbS_{0.84}Te_{0.16}$ nanomaterials obtained through thermodynamic phase segregation: $\sim 2 \times 10^4$ S m^{-1} at 700 K.[69]

While in the present work PbTe and PbS phases were not intentionally doped, a doping-like effect occurred when mixing both semiconductors at the nanometer scale.[38−40] This nanocrystal-based doping translated into larger electrical conductivities but slightly lower absolute values of the Seebeck coefficient (Figures 11, 12).

Thermal Conductivity. Thermal conductivity values were calculated from thermal diffusivities obtained using flash diffusivity measurements. In nanomaterials, when calculating thermal conductivity from thermal diffusivity data, the surface contribution to the molar heat capacity needs to be taken into account.[70] Heat capacities were measured by a relaxation method. As expected, the experimental heat capacity values obtained from $(PbTe)_{1-x}(PbS)_x$ nanomaterials significantly exceeded the Dulong−Petit approximation (SI, Figure S5). However, surprisingly lower heat capacity values were obtained for nanocomposites when compared to pure nanomaterials. The thermal conductivities

calculated from experimental heat capacities are displayed in Figure 13A. Very low thermal conductivities were obtained for all the nanomaterials characterized. These low thermal conductivity values were in part associated with the material porosity. The porosity contribution could be roughly estimated and removed from the calculated thermal conductivities using Maxwell-Eucken's equation (SI).[71−74] Figure 13B displays the porosity-corrected thermal conductivities (κ*). Taking into account the intrinsic character of the two material components, the electronic contribution to the thermal conductivity (k_e*) was calculated using the Wiedemann−Franz (WF) law assuming the nondegenerated limit for the Lorenz number (1.5×10^{-8} W Ω K^{-2}).[18,21,75,76]

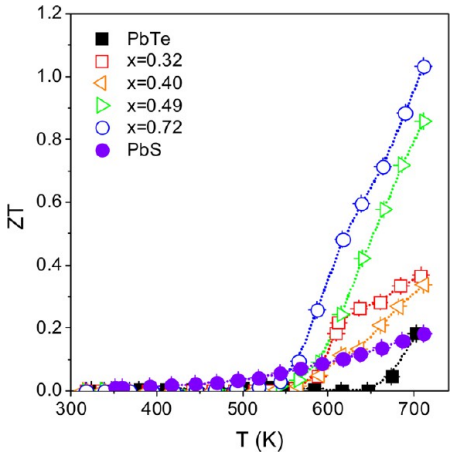

Figure 14. Thermoelectric figure of merit (ZT) of $(PbTe)_{1-x}(PbS)_x$ nanomaterials.

After porosity correction, thermal conductivities were still exceptionally low.[18,69] The thermal conductivity of the pure PbTe nanomaterial was 1.2 W/mK at 700 K. Thermal conductivity monotonically decreased with the concentration of PbS in $(PbTe)_{1-x}(PbS)_x$ nanocomposites (Figure 12). The lowest thermal conductivity, 0.53 W m^{-1} k^{-1}, was obtained for $(PbTe)_{0.28}(PbS)_{0.72}$ at 710 K. Slightly higher thermal conductivities were obtained for PbS: 0.77 W m^{-1} k^{-1} at 709 K. This value still represents a strong reduction with respect to the 1.5 W m^{-1} k^{-1} at 730 K reported for bulk PbS.

The very low thermal conductivities obtained were associated with the efficient scattering of phonons at the high density of grain boundaries and crystal interfaces within the $(PbTe)_{1-x}(PbS)_x$ nanomaterials. In nanocomposites, phonon scattering was further enhanced by the acoustic impedance mismatch between PbTe and PbS phases. The incoherent nature of

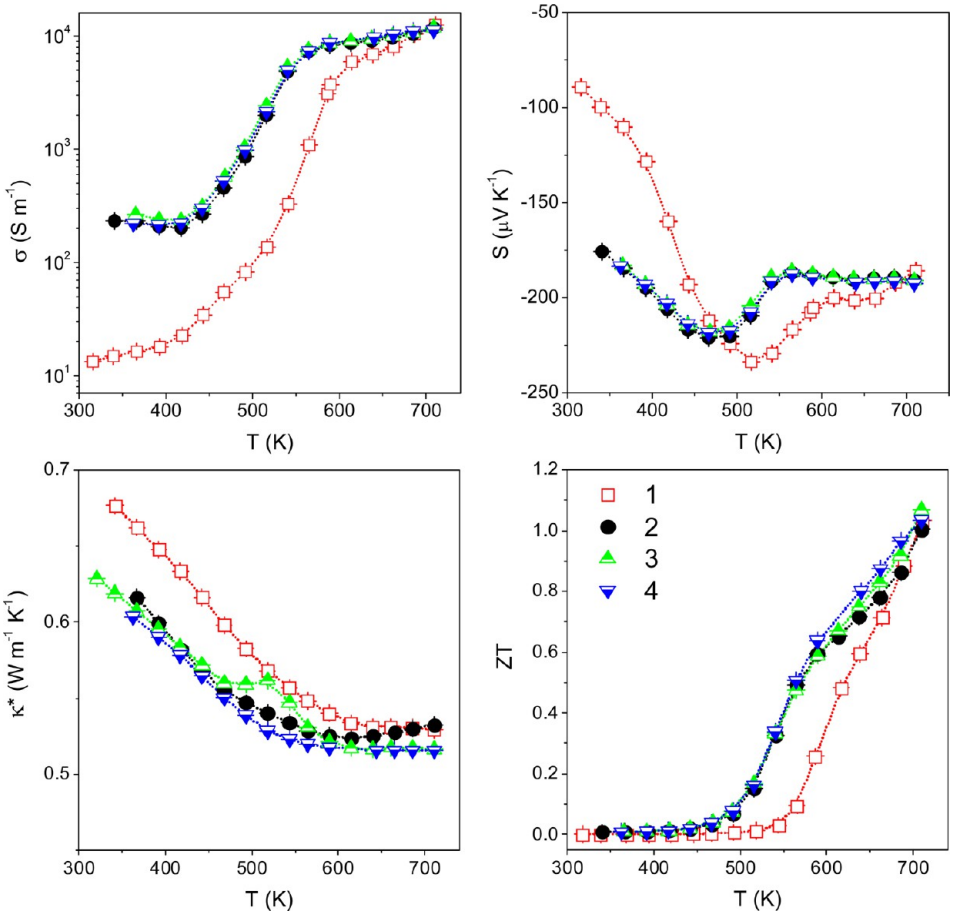

Figure 15. Multiple measurements of the electrical conductivity (σ), thermopower (S), porosity-corrected thermal conductivity (κ*), and thermoelectric figure of merit (ZT) from the same $(PbTe)_{0.28}(PbS)_{0.72}$ pellet.

interfaces in bottom-up-assembled nanocomposites additionally enhanced phonon scattering efficiency. Another parameter that may contribute to phonon scattering within the produced $(PbTe)_{1-x}(PbS)_x$ nanocomposites is the partial phase alloying detected. Alloying or replacement of Te by S ions in PbTe and of S by Te ions in PbS introduced high densities of point defects. Taking into account the large difference in size between Te and S ions, such replacement may effectively scatter short-wavelength phonons and thus contribute to further reduce the nanocomposite thermal conductivity. Phase alloying was stronger the larger the concentration of sulfur in the nanocomposite. This experimental observation partially explains the decrease of thermal conductivity with the increase of the PbS content.

Thermoelectric Figure of Merit. Figure 14 displays the thermoelectric figure of merit calculated for the different $(PbTe)_{1-x}(PbS)_x$ nanomaterials. The maximum ZT value for pure PbTe and PbS nanostructured material obtained was 0.18 at 700 K. A similar thermoelectric figure of merit was reported for undoped bulk PbS.[21] Nanocomposites obtained from core−shell NPs were characterized by figures of merit substantially higher than those of pure PbTe and PbS nanomaterials. From the compositions studied here, the nanocomposite with the largest figure of merit was $(PbTe)_{0.28}(PbS)_{0.72}$. For this nanocomposite a figure of merit ZT up to 1.07 at 700 K was calculated. The larger figures of merit obtained for nanocomposites when compared to pure nanomaterials were attributed to two main effects: (i) a synergic effect between the charge carriers of each phase resulted in nanocomposites with electrical conductivities up to 1 order of magnitude higher than pure materials; (ii) enhanced phonon scattering at multiple length scales provided nanocomposites with significantly lower thermal conductivities.

Nanomaterials' stability and measurement reproducibility are major concerns, particularly in bottom-up-assembled nanocomposites. We tested the thermoelectric performance stability of the nanocomposites by measuring the materials' thermoelectric properties multiple times on different days. Figure 15 displays data obtained from measuring the thermoelectric properties of $(PbTe)_{0.28}(PbS)_{0.72}$ four times. We observed that after the first measurement higher electrical conductivities and Seebeck coefficients and lower thermal conductivities were obtained in the low-temperature range. After the second measurement, thermoelectric properties remained unchanged. We hypothesize that changes between the first and next cycles may have its origin in a slight loss of sulfur.[77] At above 500 K small amounts of S may leave the PbS surface during the measurement. The result of such migration is a slight increase of the free electrons' concentration and thus of the electrical conductivity. The concentration of sulfur in the surface may be stabilized after the first measurement as further measurements did not show appreciable changes at either high or low temperatures. It must be pointed out that such potential sulfur loss was not detected by ICP or EDX.

CONCLUSION

A rapid, high-yield, and scalable colloidal synthetic route to prepare PbTe@PbS core−shell NPs with unprecedented narrow size distributions and exceptional control over their composition was presented. $(PbTe)_{1-x}(PbS)_x$ nanocomposites obtained from the bottom-up assembly of $(PbTe)_{1-x}$@$(PbS)_x$ NPs were highly homogeneous at the micrometer scale but contained a high distribution of nanoscale inhomogeneities. These $(PbTe)_{1-x}(PbS)_x$ nanocomposites were characterized by higher electrical conductivities and lower thermal conductivities than pure PbTe and PbS nanomaterials. We associated the higher electrical conductivities with a nanocrystal-based doping effect. The lower thermal conductivities were explained by the acoustic impedance mismatch between PbTe and PbS phases, the incoherent nature of interfaces, and the partial phase alloying. As a result, we obtained nanocomposites with thermoelectric figures of merit much higher than pure PbTe and PbS nanomaterials.

The design and engineering of nanocomposites by the bottom-up assembly of colloidal building blocks is a very recent research field. A lot of effort is still needed to optimize and completely understand the performance and properties of the nanomaterials produced by this method. However, the high thermoelectric figures of merit obtained here serve as an example of the potential of the proposed processes to produce high-performing nanomaterials. It also allows establishing the bottom-up assembly of colloidal NPs as a serious approach to produce functional nanocomposites with unprecedented and unparallel control over material phase and composition at the nanometer scale.

MATERIALS AND METHODS

Chemicals. Lead(II) oxide (99.9%), oleic acid (OA, tech. 90%), 1-octadecene (ODE, 90%), tellurium shots (99.999%), thioacetamide (ACS reagent, ≥99.0%), hexamethyldisilathiane (TMS_2S, synthesis grade), and *N*,*N*-dimethylformamide (DMF, ≥99%) were purchased from Aldrich. Tri-*n*-octylphosphine (TOP, 97%) was purchased from Strem. Methanol, acetone, hexane, chloroform, and ethanol were of analytical grade and obtained from various sources. All chemicals were used as received without further purification. All syntheses were carried out using standard airless techniques: a vacuum/dry argon gas Schlenk line was used for the synthesis and an argon glovebox for storing and handling air- and moisture-sensitive chemicals.

Preparation of PbS NPs. A modified approach of that used by Hines *et al.*[78] was used for the preparation of PbS nanocrystals. Lead(II) oxide (2.94 g, 12 mM) and oleic acid (90 mL, 48 mM)

were dissolved in 90 mL of ODE. This mixture was degassed at RT and 100 °C for 0.5 h each to form a lead oleate complex. Afterward, the transparent solution was flashed with argon and heated to the reaction temperature (135 °C). At this temperature, 1.26 mL of TMS_2S dissolved in 40 mL of ODE was rapidly injected under argon gas flow. For the crystal growth the reaction mixture was kept for 3 more min and then quickly cooled to room temperature using a water bath.

Preparation of PbTe NPs. A modified approach of that used by Murphy *et al.*[79] was used for the preparation of PbTe nanocrystals. In a typical procedure, PbO (2.94 g, 12 mM) and OA (13.32 g, 4.75 mM) were dissolved in 90 mL of ODE. This mixture was degassed at RT and 100 °C for 0.5 h each to form a lead oleate complex. The solution was flushed with Ar, and the temperature was raised to 190 °C. Afterward 2 mL of 1 M TOP:Te was rapidly injected. The reaction mixture was maintained between 160 and 180 °C for 3 min and then quickly cooled to room temperature using a water bath. At this point an aliquot was extracted to analyze the PbTe morphology.

Preparation of PbTe@PbS NPs with a Crystalline PbS Shell. Once the crude solution containing the PbTe NP was at room temperature, 114 mg of thioacetamide dissolved in 6 mL of DMF was added into the flask. The NP solution containing the sulfur precursor was heated to 80 °C at 1.7 °C/min and maintained at this temperature for 30 min. After cooling to room temperature, the NPs were precipitated by centrifugation.

Preparation of PbTe@PbS NPs with an Amorphous PbS Shell. In this case, the cooling procedure of the PbTe NP crude solution was stopped at 80 °C; then the sulfur precursor (114 mg of thioacetamide dissolved in 6 mL of DMF) was injected. The NP solution containing the sulfur precursor was maintained at 80 °C for an additional 5 min. After cooling to room temperature, the NPs were precipitated by centrifugation.

Preparation of PbTe−PbS Nanocomposites. The obtained PbTe@PbS NPs were thoroughly washed by multiple precipitation and redispersion steps, until they could not be redispersed in organic solvents. At this point, most of the surfactants initially used to control the nanoparticle size, shape, and solubility had been already removed. Washed NPs were dried out under an Ar atmosphere. Afterward, the nanocrystals were heated to 500 °C for 2 h under an Ar flow inside a tube furnace. The resulting material was pressed into pellets (10 mm diameter; 1 mm thickness) under a load of 2 tons at room temperature. All the pellets used in this study present densities around 80% with respect to their theoretical value. To estimate the density value, we performed geometric measurements and weighed all the pellets accurately. Using the percentage of PbS and PbTe present, we calculate the expected theoretical density for each pellet.

Structural and Chemical Characterization. The samples were analyzed by means of HRTEM in a Jeol 2010F field emission gun microscope operated at 200 kV. Nanoparticle core−shell atomic models were created by using the Rhodius software,[80] widely used to model NW complex nanostructures.[81−83]

Thermoelectric Characterization. The samples used to measure the electrical conductivity and the Seebeck coefficient were rectangular parallelepipeds of about 10 × 13 × 1 mm^3. The Seebeck coefficient was measured using a static DC method. Electrical resistivity data were obtained by the standard four-probe method. Both the Seebeck coefficient and electrical resistivity were measured simultaneously in a LSR-3 LINSEIS system in the range between room temperature and 700 K, under a helium atmosphere. The temperature dependence of the heat capacity was measured by a relaxation method using a Quantum Design physical properties measurement system (PPMS). Thermal conductivity measurements were obtained from flash diffusivity measurements in a Netzsch LFA-457 Microflash.

Conflict of Interest: The authors declare no competing financial interest.

Supporting Information Available: Complementary XRD patterns, TEM micrographs, SEM images, XPS measurements, thermogravimetry analysis, and heat capacity measurements. This material is available free of charge *via* the Internet at http://pubs.acs.org

Acknowledgment. The research was supported by the European Regional Development Funds (ERDF, "FEDER Programa Competitivitat de Catalunya 2007-2013") and the Spanish MICINN Projects MAT2008-05779, MAT2010-15138, CSD2009-00050, and CSD2009-00013. M.I. thanks the Spanish MICINN for her Ph.D. grant. J.A. and R.Z. also acknowledge Generalitat de Catalunya 2009-SGR-770 and XaRMAE.

REFERENCES AND NOTES

1. Yin, Y.; Alivisatos, A. P. Colloidal Nanocrystal Synthesis and the Organic-Inorganic Interface. *Nature* **2005**, *437*, 664–670.
2. Talapin, D. V.; Lee, J.-S.; Kovalenko, M. V.; Shevchenko, E. V. Prospects of Colloidal Nanocrystals for Electronic and Optoelectronic Applications. *Chem. Rev.* **2010**, *110*, 389–458.
3. Ibáñez, M.; Zamani, R.; Li, W.; Shavel, A.; Arbiol, J.; Morante, J. R.; Cabot, A. Extending the Nanocrystal Synthesis Control to Quaternary Compositions. *Cryst. Growth Des.* **2012**, *12*, 1085–1090.
4. Li, W.; Shavel, A.; Guzman, R.; Rubio-Garcia, J.; Flox, C.; Fan, J.; Cadavid, D.; Ibáñez, M.; Arbiol, J.; Morante, J. R.; *et al.* Morphology Evolution of $Cu_{(2-x)}S$ Nanoparticles: from Spheres to Dodecahedrons. *Chem. Commun.* **2011**, *47*, 10332–10334.
5. Ibáñez, M.; Guardia, P.; Shavel, A.; Cadavid, D.; Arbiol, J.; Morante, J. R.; Cabot, A. Growth Kinetics of Asymmetric Bi_2S_3 Nanocrystals: Size Distribution Focusing in Nanorods. *J. Phys. Chem. C* **2011**, *115*, 7947–7955.
6. Jun, Y.-W.; Choi, J.-S.; Cheon, J. Shape Control of Semiconductor and Metal Oxide Nanocrystals through Nonhydrolytic Colloidal Routes. *Angew. Chem., Int. Ed.* **2006**, *45*, 3414–3439.
7. Hicks, L. D.; Dresselhaus, M. S. Effect of Quantum-Well Structures on the Thermoelectric Figure of *Merit. Phys. Rev. B* **1993**, *47*, 12727–12731.
8. Hicks, L. D.; Harman, T. C.; Dresselhaus, M. S. Use of Quantum-Well Superlattices to Obtain a High Figure of Merit from Nonconventional Thermoelectric Materials. *Appl. Phys. Lett.* **1993**, *63*, 3230–3232.
9. Humphrey, T. E.; Linke, H. Reversible Thermoelectric Nanomaterials. *Phys. Rev. Lett.* **2005**, *94*, 096601.
10. Zide, J. M. O.; Vashaee, D.; Bian, Z. X.; Zeng, G.; Bowers, J. E.; Shakouri, A.; Gossard, A. C. Demonstration of Electron Filtering to Increase the Seebeck Coefficient in $In_{0.53}Ga_{0.47}As/In_{0.53}Ga_{0.28}Al_{0.19}As$ Superlattices. *Phys. Rev. B* **2006**, *74*, 205335.
11. Vashaee, D.; Shakouri, A. Improved Thermoelectric Power Factor in Metal-Based Superlattices. *Phys. Rev. Lett.* **2004**, *92*, 106103.
12. Faleev, S. V.; Léonard, F. Theory of Enhancement of Thermoelectric Properties of Materials with Nanoinclusions. *Phys. Rev. B* **2008**, *77*, 214304.
13. Martin, J.; Wang, L.; Chen, L.; Nolas, G. S. Enhanced Seebeck Coefficient through Energy-Barrier Scattering in PbTe Nanocomposites. *Phys. Rev. B* **2009**, *79*, 115311.
14. Harman, T. C.; Taylor, P. J.; Walsh, M. P.; LaForge, B. E. Quantum Dot Superlattice Thermoelectric Materials and Devices. *Science* **2002**, *297*, 2229–2232.
15. Venkatasubramanian, R.; Siivola, E.; Colpitts, T.; O'Quinn, B. Thin-Film Thermoelectric Devices with High Room-Temperature Figures of Merit. *Nature* **2001**, *413*, 597–602.
16. Pei, Y.; Lensch-Falk, J.; Toberer, E. S.; Medlin, D. L.; Snyder, G. J. High Thermoelectric Performance in PbTe Due to Large Nanoscale Ag_2Te Precipitates and La Doping. *Adv. Funct. Mater.* **2010**, *21*, 241–249.
17. Biswas, K.; He, J.; Wang, G.; Lo, S.-H.; Uher, C.; Dravid, V. P.; Kanatzidis, M. G. High Thermoelectric Figure of Merit in Nanostructured p-Type PbTe-MTe (M = Ca, Ba). *Energy Environ. Sci.* **2011**, *4*, 4675–4684.
18. Girard, S. N.; He, J.; Zhou, X.; Shoemaker, D.; Jaworski, C. M.; Uher, C.; Dravid, V. P.; Heremans, J. P.; Kanatzidis, M. G. High Performance Na-Doped PbTe-PbS Thermoelectric Materials: Electronic Density of States Modification and Shape-Controlled Nanostructures. *J. Am. Chem. Soc.* **2011**, *133*, 16588–16597.

19. Androulakis, J.; Lin, C.-H.; Kong, H.-J.; Uher, C.; Wu, C.-I.; Hogan, T.; Cook, B. A.; Caillat, T.; Paraskevopoulos, K. M.; Kanatzidis, M. G. Spinodal Decomposition and Nucleation and Growth as a Means to Bulk Nanostructured Thermoelectrics: Enhanced Performance in $Pb_{1-x}Sn_xTe$-PbS. *J. Am. Chem. Soc.* **2007**, *129*, 9780–9788.
20. Girard, S. N.; He, J.; Li, C.; Moses, S.; Wang, G.; Uher, C.; Dravid, V. P.; Kanatzidis, M. G. *In Situ* Nanostructure Generation and Evolution within a Bulk Thermoelectric Material to Reduce Lattice Thermal Conductivity. *Nano Lett.* **2010**, *10*, 2825–2831.
21. Zhao, L.-D.; Lo, S.-H.; He, J.; Li, H.; Biswas, K.; Androulakis, J.; Wu, C.-I.; Hogan, T. P.; Chung, D.-Y.; Dravid, V. P.; *et al*. High Performance Thermoelectrics from Earth-Abundant Materials: Enhanced Figure of Merit in PbS by Second Phase Nanostructures. *J. Am. Chem. Soc.* **2011**, *133*, 20476–20487.
22. Zhao, L.-D.; He, J.; Wu, C.-I.; Hogan, T. P.; Zhou, X.; Uher, C.; Dravid, V. P.; Kanatzidis, M. G. Thermoelectrics with Earth Abundant Elements: High Performance p-Type PbS Nanostructured with SrS and CaS. *J. Am. Chem. Soc.* **2012**, *134*, 7902–7912.
23. Girard, S. N.; Schmidt-Rohr, K.; Chasapis, T. C.; Hatzikraniotis, E.; Njegic, B.; Levin, E. M.; Rawal, A.; Paraskevopoulos, K. M.; Kanatzidis, M. G. Analysis of Phase Separation in High Performance PbTe–PbS Thermoelectric Materials. *Adv. Funct. Mater.* **2013**, *23*, 747–757.
24. Mehta, R. J.; Zhang, Y.; Karthik, C.; Singh, B.; Siegel, R. W.; Borca-Tasciuc, T.; Ramanath, G. A New Class of Doped Nanobulk High-Figure-of-Merit Thermoelectrics by Scalable Bottom-up Assembly. *Nat. Mater.* **2012**, *11*, 233–240.
25. Kovalenko, M. V.; Spokoyny, B.; Lee, J. S.; Scheele, M.; Weber, A.; Perera, S.; Landry, D.; Talapin, D. V. Semiconductor Nanocrystals Functionalized with Antimony Telluride Zintl Ions for Nanostructured Thermoelectrics. *J. Am. Chem. Soc.* **2010**, *132*, 6686–6695.
26. Scheele, M.; Oeschler, N.; Meier, K.; Kornowski, A.; Klinke, C.; Weller, H. Synthesis and Thermoelectric Characterization of Bi_2Te_3 Nanoparticles. *Adv. Funct. Mater.* **2009**, *19*, 3476–3483.
27. Scheele, M.; Oeschler, N.; Veremchuk, I.; Peters, S. O.; Littig, A.; Kornowski, A.; Klinke, C.; Weller, H. Thermoelectric Properties of Lead Chalcogenide Core-Shell Nanostructures. *ACS Nano* **2011**, *5*, 8541–8551.
28. Scheele, M.; Oeschler, N.; Veremchuk, I.; Reinsberg, K. G.; Kreuziger, A. M.; Kornowski, A.; Broekaert, J.; Klinke, C.; Weller, H. ZT Enhancement in Solution-Grown $Sb_{(2-x)}Bi_xTe_3$ Nanoplatelets. *ACS Nano* **2010**, *4*, 4283–4291.
29. Ibáñez, M.; Zamani, R.; Lalonde, A.; Cadavid, D.; Li, W.; Shavel, A.; Arbiol, J.; Morante, J. R.; Gorsse, S.; Snyder, G. J.; *et al*. $Cu_2ZnGeSe_4$ Nanocrystals: Synthesis and Thermoelectric Properties. *J. Am. Chem. Soc.* **2012**, *134*, 4060–4063.
30. Ibáñez, M.; Zamani, R.; Li, W.; Cadavid, D.; Gorsse, S.; Katcho, N. A.; Shavel, A.; López, A. M.; Morante, J. R.; Arbiol, J.; *et al*. Crystallographic Control at the Nanoscale To Enhance Functionality: Polytypic Cu_2GeSe_3 Nanoparticles as Thermoelectric Materials. *Chem. Mater.* **2012**, *24*, 4615–4622.
31. Ibáñez, M.; Cadavid, D.; Zamani, R.; García-Castelló, N.; Izquierdo-Roca, V.; Li, W.; Fairbrother, A.; Prades, J. D.; Shavel, A.; Arbiol, J.; *et al*. Composition Control and Thermoelectric Properties of Quaternary Chalcogenide Nanocrystals: The Case of Stannite $Cu_2CdSnSe_4$. *Chem. Mater.* **2012**, *24*, 562–570.
32. Ibáñez, M.; Cadavid, D.; Anselmi Tamburini, U.; Zamani, R.; Gorsse, S.; Li, W.; Shavel, A.; López, A. M.; Morante, J. R.; Arbiol, J.; *et al*. Colloidal Synthesis and Thermoelectric Properties of Cu_2SnSe_3 Nanocrystals. *J. Mater. Chem. A* **2013**, *1*, 1421.
33. Cadavid, D.; Ibáñez, M.; Gorsse, S.; López, A. M.; Cirera, A.; Morante, J.; Cabot, A. Bottom-up Processing of Thermoelectric Nanocomposites from Colloidal Nanocrystal Building Blocks: The Case of Ag_2Te-PbTe. *J. Nanopart. Res.* **2012**, *14*, 1–10.
34. Lee, J.-S.; Bodnarchuk, M. I.; Shevchenko, E. V.; Talapin, D. V. "Magnet-in-the-Semiconductor" FePt-PbS and FePt-PbSe Nanostructures: Magnetic Properties, Charge Transport, and Magnetoresistance. *J. Am. Chem. Soc.* **2010**, *132*, 6382–6391.
35. Lee, J.-S.; Shevchenko, E. V.; Talapin, D. V. Au-PbS Core-Shell Nanocrystals: Plasmonic Absorption Enhancement and Electrical Doping *via* Intra-Particle Charge Transfer. *J. Am. Chem. Soc.* **2008**, *130*, 9673–9675.
36. Shevchenko, E. V.; Ringler, M.; Schwemer, A.; Talapin, D. V.; Klar, T. A.; Rogach, A. L.; Feldmann, J.; Alivisatos, A. P. Self-Assembled Binary Superlattices of CdSe and Au Nanocrystals and Their Fluorescence Properties. *J. Am. Chem. Soc.* **2008**, *130*, 3274–3275.
37. Talapin, D. V.; Shevchenko, E. V.; Bodnarchuk, M. I.; Ye, X.; Chen, J.; Murray, C. B. Quasicrystalline Order in Self-Assembled Binary Nanoparticle Superlattices. *Nature* **2009**, *461*, 964–967.
38. Urban, J. J.; Talapin, D. V.; Shevchenko, E. V.; Kagan, C. R.; Murray, C. B. Synergism in Binary Nanocrystal Superlattices Leads to Enhanced p-Type Conductivity in Self-Assembled PbTe/Ag_2Te Thin Films. *Nat. Mater.* **2007**, *6*, 115–121.
39. Hanrath, T. Colloidal Nanocrystal Quantum Dot Assemblies as Artificial Solids. *J. Vac. Sci. Technol. A* **2012**, *30*, 030802.
40. Ko, D.-K.; Urban, J. J.; Murray, C. B. Carrier Distribution and Dynamics of Nanocrystal Solids Doped with Artificial Atoms. *Nano Lett.* **2010**, *10*, 1842–1847.
41. Reiss, P.; Bleuse, J.; Pron, A. Highly Luminescent CdSe/ZnSe Core/Shell Nanocrystals of Low Size Dispersion. *Nano Lett.* **2002**, *2*, 781–784.
42. Peng, X.; Schlamp, M. C.; Kadavanich, A. V.; Alivisatos, A. P. Epitaxial Growth of Highly Luminescent CdSe/CdS Core/Shell Nanocrystals with Photostability and Electronic Accessibility. *J. Am. Chem. Soc.* **1997**, *119*, 7019–7029.
43. Chalkidou, A.; Simeonidis, K.; Angelakeris, M.; Samaras, T.; Martinez-Boubeta, C.; Balcells, L.; Papazisis, K.; Dendrinou-Samara, C.; Kalogirou, O. *In Vitro* Application of Fe/MgO Nanoparticles as Magnetically Mediated Hyperthermia Agents for Cancer Treatment. *J. Magn. Magn. Mater.* **2011**, *323*, 775–780.
44. Gerion, D.; Pinaud, F.; Williams, S. C.; Parak, W. J.; Zanchet, D.; Weiss, S.; Alivisatos, A. P. Synthesis and Properties of Biocompatible Water-Soluble Silica-Coated CdSe/ZnS Semiconductor Quantum Dots. *J. Phys. Chem. B* **2001**, *105*, 8861–8871.
45. Wise, F. W. Lead Salt Quantum Dots: The Limit of Strong Quantum Confinement. *Acc. Chem. Res.* **2000**, *33*, 773–780.
46. Talapin, D. V.; Murray, C. B. PbSe Nanocrystal Solids for n- and p-Channel Thin Film Field-Effect Transistors. *Science* **2005**, *310*, 86–89.
47. Konstantatos, G.; Howard, I.; Fischer, A.; Hoogland, S.; Clifford, J.; Klem, E.; Levina, L.; Sargent, E. H. Ultrasensitive Solution-Cast Quantum Dot Photodetectors. *Nature* **2006**, *442*, 180–183.
48. McDonald, S. A.; Konstantatos, G.; Zhang, S.; Cyr, P. W.; Klem, E. J. D.; Levina, L.; Sargent, E. H. Solution-Processed PbS Quantum Dot Infrared Photodetectors and Photovoltaics. *Nat. Mater.* **2005**, *4*, 138–142.
49. Choi, J. J.; Lim, Y.-F.; Santiago-Berrios, M. E. B.; Oh, M.; Hyun, B.-R.; Sun, L.; Bartnik, A. C.; Goedhart, A.; Malliaras, G. G.; Abruña, H. c. D.; *et al*. PbSe Nanocrystal Excitonic Solar Cells. *Nano Lett.* **2009**, *9*, 3749–3755.
50. Pattantyus-Abraham, A. G.; Kramer, I. J.; Barkhouse, A. R.; Wang, X.; Konstantatos, G.; Debnath, R.; Levina, L.; Raabe, I.; Nazeeruddin, M. K.; Grätzell, M.; *et al*. Depleted-Heterojunction Colloidal Quantum Dot Solar Cells. *ACS Nano* **2010**, *4*, 3374–3380.
51. Ma, W.; Luther, J. M.; Zheng, H.; Wu, Y.; Alivisatos, A. P. Photovoltaic Devices Employing Ternary PbS_xSe_{1-x} Nanocrystals. *Nano Lett.* **2009**, *9*, 1699–1703.
52. Tang, J.; Liu, H.; Zhitomirsky, D.; Hoogland, S.; Wang, X.; Furukawa, M.; Levina, L.; Sargent, E. H. Quantum Junction Solar Cells. *Nano Lett.* **2012**, *12*, 4889–4894.
53. Koleilat, G. I.; Levina, L.; Shukla, H.; Myrskog, S. H.; Hinds, S.; Pattantyus-Abraham, A. G.; Sargent, E. H. Efficient, Stable

Infrared Photovoltaics Based on Solution-Cast Colloidal Quantum Dots. *ACS Nano* **2008**, *2*, 833–840.
54. Luther, J. M.; Law, M.; Beard, M. C.; Song, Q.; Reese, M. O.; Ellingson, R. J.; Nozik, A. J. Schottky Solar Cells Based on Colloidal Nanocrystal Films. *Nano Lett.* **2008**, *8*, 3488–3492.
55. Hoogland, S.; Sukhovatkin, V.; Howard, I.; Cauchi, S.; Levina, L.; Sargent, E. H. A Solution-Processed 1.53 um Quantum Dot Laser with Temperature-Invariant Emission Wavelength. *Opt. Express* **2006**, *14*, 3273–3281.
56. Michalet, X.; Pinaud, F. F.; Bentolila, L. A.; Tsay, J. M.; Doose, S.; Li, J. J.; Sundaresan, G.; Wu, A. M.; Gambhir, S. S.; Weiss, S. Quantum Dots for Live Cells, in Vivo Imaging, and Diagnostics. *Science* **2005**, *307*, 538–544.
57. Gill, R.; Zayats, M.; Willner, I. Semiconductor Quantum Dots for Bioanalysis. *Angew. Chem., Int. Ed.* **2008**, *47*, 7602–7625.
58. Klem, E. J. D.; MacNeil, D. D.; Levina, L.; Sargent, E. H. Solution Processed Photovoltaic Devices with 2% Infrared Monochromatic Power Conversion Efficiency: Performance Optimization and Oxide Formation. *Adv. Mater.* **2008**, *20*, 3433–3439.
59. Zhao, Y.; Burda, C. Chemical Synthesis of $Bi_{0.5}Sb_{1.5}Te_3$ Nanocrystals and Their Surface Oxidation Properties. *ACS Appl. Mater. Interfaces* **2009**, *1*, 1259–1263.
60. Mokari, T.; Zhang, M.; Yang, P. Shape, Size, and Assembly Control of PbTe Nanocrystals. *J. Am. Chem. Soc.* **2007**, *129*, 9864–9865.
61. Zyubina, T. S.; Neudachina, V. S.; Yashina, L. V.; Shtanov, V. I. XPS and *ab Initio* Study of the Interaction of PbTe with Molecular Oxygen. *Surf. Sci.* **2005**, *574*, 52–64.
62. Yashina, L. V.; Zyubina, T. S.; Püttner, R.; Zyubin, A. S.; Shtanov, V. I.; Tikhonov, E. V. A Combined Photoelectron Spectroscopy and *ab Initio* Study of the Adsorbate System O_2/PbTe(001) and the Oxide Layer Growth Kinetics. *J. Phys. Chem. C* **2008**, *112*, 19995–20006.
63. Fu, H.; Tsang, S.-W.; Zhang, Y.; Ouyang, J.; Lu, J.; Yu, K.; Tao, Y. Impact of the Growth Conditions of Colloidal PbS Nanocrystals on Photovoltaic Device Performance. *Chem. Mater.* **2011**, *23*, 1805–1810.
64. Zhang, H.; Hu, B.; Sun, L.; Hovden, R.; Wise, F. W.; Muller, D. A.; Robinson, R. D. Surfactant Ligand Removal and Rational Fabrication of Inorganically Connected Quantum Dots. *Nano Lett.* **2011**, *11*, 5356–5361.
65. Gyorffy, B. L. Coherent-Potential Approximation for a Nonoverlapping-Muffin-Tin-Potential Model of Random Substitutional Alloys. *Phys. Rev. B* **1972**, *5*, 2382–2384.
66. Soven, P. Coherent-Potential Model of Substitutional Disordered Alloys. *Phys. Rev.* **1967**, *156*, 809–813.
67. Volykhov, A.; Yashina, L.; Shtanov, V. Phase Relations in Pseudobinary Systems of Germanium, Tin, and Lead Chalcogenides. *Inorg. Mater.* **2006**, *42*, 596–604.
68. Seto, J. Y. W. The Electrical Properties of Polycrystalline Silicon Films. *J. Appl. Phys.* **1975**, *46*, 5247–5254.
69. Johnsen, S.; He, J.; Androulakis, J.; Dravid, V. P.; Todorov, I.; Chung, D. Y.; Kanatzidis, M. G. Nanostructures Boost the Thermoelectric Performance of PbS. *J. Am. Chem. Soc.* **2011**, *133*, 3460–3470.
70. Rupp, J.; Birringer, R. Enhanced Specific-Heat-Capacity (C_p) Measurements (150−300 K) of Nanometer-Sized Crystalline Materials. *Phys. Rev. B* **1987**, *36*, 7888–7890.
71. Carson, J. K.; Lovatt, S. J.; Tanner, D. J.; Cleland, A. C. Thermal Conductivity Bounds for Isotropic, Porous Materials. *Int. J. Heat Mass Transfer* **2005**, *48*, 2150–2158.
72. Ondracek, G.; Schulz, B. The Porosity Dependence of the Thermal Conductivity for Nuclear Fuels. *J. Nucl. Mater.* **1973**, *46*, 253–258.
73. Adachi, J.; Kurosaki, K.; Uno, M.; Yamanaka, S. Effect of Porosity on Thermal and Electrical Properties of Polycrystalline Bulk ZrN Prepared by Spark Plasma Sintering. *J. Alloys Compd.* **2007**, *432*, 7–10.
74. Yang, L.; Wu, J. S.; Zhang, L. T. Synthesis of Filled Skutterudite Compound $La_{0.75}Fe_3CoSb_{12}$ by Spark Plasma Sintering and Effect of Porosity on Thermoelectric Properties. *J. Alloys Compd.* **2004**, *364*, 83–88.
75. Biswas, K.; He, J.; Blum, I. D.; Wu, C.-I.; Hogan, T. P.; Seidman, D. N.; Dravid, V. P.; Kanatzidis, M. G. High-Performance Bulk Thermoelectrics with All-Scale Hierarchical Architectures. *Nature* **2012**, *489*, 414–418.
76. May, A. F.; Fleurial, J.-P.; Snyder, G. J. Thermoelectric Performance of Lanthanum Telluride Produced *via* Mechanical Alloying. *Phys. Rev. B* **2008**, *78*, 125205.
77. Scanlon, W. W. Interpretation of Hall Effect and Resistivity Data in PbS and Similar Binary Compound Semiconductors. *Phys. Rev.* **1953**, *92*, 1573–1575.
78. Hines, M. A.; Scholes, G. D. Colloidal PbS Nanocrystals with Size-Tunable Near-Infrared Emission: Observation of Post-Synthesis Self-Narrowing of the Particle Size Distribution. *Adv. Mater.* **2003**, *15*, 1844–1849.
79. Murphy, J. E.; Beard, M. C.; Norman, A. G.; Ahrenkiel, S. P.; Johnson, J. C.; Yu, P.; Mićić, O. I.; Ellingson, R. J.; Nozik, A. J. PbTe Colloidal Nanocrystals: Synthesis, Characterization, and Multiple Exciton Generation. *J. Am. Chem. Soc.* **2006**, *128*, 3241–3247.
80. Bernal, S.; Botana, F. J.; Calvino, J. J.; López-Cartes, C.; Pérez-Omil, J. A.; Rodríguez-Izquierdo, J. M. The Interpretation of HRTEM Images of Supported Metal Catalysts Using Image Simulation: Profile View Images. *Ultramicroscopy* **1998**, *72*, 135–164.
81. Arbiol, J.; Cirera, A.; Peiro, F.; Cornet, A.; Morante, J. R.; Delgado, J. J.; Calvino, J. J. Optimization of Tin Dioxide Nanosticks Faceting for the Improvement of Palladium Nanocluster Epitaxy. *Appl. Phys. Lett.* **2002**, *80*, 329–331.
82. Uccelli, E.; Arbiol, J.; Morante, J. R.; Fontcuberta i Morral, A. InAs Quantum Dot Arrays Decorating the Facets of GaAs Nanowires. *ACS Nano* **2010**, *4*, 5985–5993.
83. Arbiol, J.; Magen, C.; Becker, P.; Jacopin, G.; Chernikov, A.; Schafer, S.; Furtmayr, F.; Tchernycheva, M.; Rigutti, L.; Teubert, J.; *et al.* Self-Assembled GaN Quantum Wires on GaN/AlN Nanowire Templates. *Nanoscale* **2012**, *4*, 7517–7524.